Nanoscale constraints on porosity generation and fluid flow during serpentinization

Benjamin M. Tutolo[1,2*], David F.R. Mildner[3], Cedric V.L. Gagnon[3,4], Martin O. Saar[2,5], and William E. Seyfried, Jr.[2]
[1]Department of Earth Sciences, University of Oxford, Oxford OX1 3AN, UK
[2]Department of Earth Sciences, University of Minnesota, Minneapolis, Minnesota 55455, USA
[3]National Institute of Standards and Technology Center for Neutron Research, Gaithersburg, Maryland 20899, USA
[4]Department of Materials Science and Engineering, University of Maryland, College Park, Maryland 20742, USA
[5]Department of Earth Sciences, ETH-Zürich, 8006 Zurich, Switzerland

ABSTRACT

Field samples of olivine-rich rocks are nearly always serpentinized—commonly to completion—but, paradoxically, their intrinsic porosity and permeability are diminishingly low. Serpentinization reactions occur through a coupled process of fluid infiltration, volumetric expansion, and reaction-driven fracturing. Pores and reactive surface area generated during this process are the primary pathways for fluid infiltration into and reaction with serpentinizing rocks, but the size and distribution of these pores and surface area have not yet been described. Here, we utilize neutron scattering techniques to present the first measurements of the evolution of pore size and specific surface area distribution in partially serpentinized rocks. Samples were obtained from the ca. 2 Ma Atlantis Massif oceanic core complex located off-axis of the Mid-Atlantic Ridge and an olivine-rich outcrop of the ca. 1.1 Ga Duluth Complex of the North American Mid-Continent Rift. Our measurements and analyses demonstrate that serpentine and accessory phases form with their own, inherent porosity, which accommodates the bulk of diffusive fluid flow during serpentinization and thereby permits continued serpentinization after voluminous serpentine minerals fill reaction-generated porosity.

INTRODUCTION

Olivine, the primary constituent of mantle rocks, is converted to hydrous phases when brought into contact with water at upper lithospheric temperatures (O'Hanley, 1996). This reaction, known as serpentinization, results in some of the most extreme redox and pH environments on Earth and provides nutrients for unique, chemosynthetic microbial ecosystems, which represent possible modern analogues for the origin of life on Earth (Sleep et al., 2004; Kelley et al., 2005; Seyfried et al., 2015; Klein et al., 2015).

In freshly crystallized igneous rocks, porosity exists only as small gaps between mineral grains, and the intrinsic permeability is consequently very low (Wark et al., 2003). However, textures observed within field samples indicate that serpentinization proceeds through positive feedbacks associated with reaction-driven fracturing (O'Hanley, 1996; Macdonald and Fyfe, 1985; Jamtveit et al., 2008; Kelemen and Hirth, 2012; Plümper et al., 2012), which occurs in situations where the rate of reaction is faster than the rate of solute transport away from the reacting surface. Crystallization of the voluminous secondary phases fractures the surrounding minerals and generates new porosity, permeability, and reactive surface area, and thus gives way to continued reaction of primary igneous minerals (Jamtveit et al., 2008; Kelemen and Hirth, 2012).

Because serpentinization reactions are kinetically fast (e.g., Martin and Fyfe, 1970), hydrous phase growth will rapidly infill any newly generated pore space. This would suggest that serpentinizing rocks should have essentially zero porosity at steady state, except for the brief period of time after reaction-induced fracturing occurs. However, this is evidently not the case, both because a zero-porosity rock cannot possibly permit fluid infiltration and further serpentinization (and therefore the serpentinization process would stop after the initial cracking episode), and also because measurements indicate that serpentinized peridotites indeed have nonzero porosities (e.g., Saad, 1969; Blackman et al., 2006). This latter observation has not been effectively implemented into geochemical models of serpentinization, which will inevitably calculate decreased densities of the solid reaction products relative to the primary igneous minerals. If interpreted literally, these volume-based models will always lead to the impossible inference that serpentinizing rocks have zero (or negative) porosity and permeability, even when reaction-driven fracturing is considered. Thus, a mechanistic understanding of the evolution of porosity during serpentinization is required to improve our understanding of the serpentinization process.

METHODS

Neutron scattering has offered unmatched insight into coupled hydrogeochemical processes occurring in sedimentary and igneous rocks (Radlinski et al., 2004; Anovitz et al., 2009; Navarre-Sitchler et al., 2013), and presents an ideal tool for studying the evolution of porosity, surface area, and fluid flow during serpentinization. For this study, partially serpentinized, olivine-rich samples were obtained from (1) International Ocean Discovery Program (IODP) borehole 1309D into the ca. 2 Ma Atlantis Massif (Blackman et al., 2006) off-axis of the Mid-Atlantic Ridge, which hosts the well-known Lost City Hydrothermal Field (Kelley et al., 2005; Seyfried et al., 2015; Figs. DR1 and DR2 in the GSA Data Repository[1]), and (2) the Bardon Peak outcrop (46°40.745′N, 92°14.180′W) of the troctolitic series of the ca. 1.1 Ga Duluth Complex of the North American Mid-Continent Rift (Weiblen and Morey, 1980; Foster and Hudleston, 1986; Fig. DR3). Samples were selected for their visible gradient in degree of serpentinization over a distance small enough that the primary igneous mineralogy can be approximated as constant. The Atlantis Massif samples (1309D-235-R-2-28-31, hereafter "235R2", and 1309D-241-R-1-13-17, hereafter "241R1") are olivine-rich troctolites that have been hydrated along grain contacts and intragranular microfractures, with localized regions of intense serpentinization (Fig. 1; Figs. DR1 and DR2; Table DR1). In the Duluth Complex samples, the majority of the fluid flow and hydration reactions were confined to millimeter-width, outcrop-scale fractures, which are entirely composed of secondary minerals, and little hydration occurred within the interfracture matrix, where secondary minerals exist primarily along grain boundaries and in sparse microfracture fillings (Fig. 1; Fig. DR3).

Samples were prepared using standard methods (Anovitz et al., 2009) and subjected to small-angle neutron scattering (SANS) measurements on the NG3 (now known as NGB30; Glinka et al., 1998) and ultra-SANS (USANS) on the BT5 (Barker et al., 2005) beamlines at the

*E-mail: benjamin.tutolo@earth.ox.ac.uk

[1]GSA Data Repository item 2016028, extended methods, including additional sample images, (U) SANS figures, and a table of chemical analyses and calculated SLDs; and a Microsoft Excel spreadsheet containing data utilized in producing Figure 2, is available online at www.geosociety.org/pubs/ft2016.htm, or on request from editing@geosociety.org or Documents Secretary, GSA, P.O. Box 9140, Boulder, CO 80301, USA.

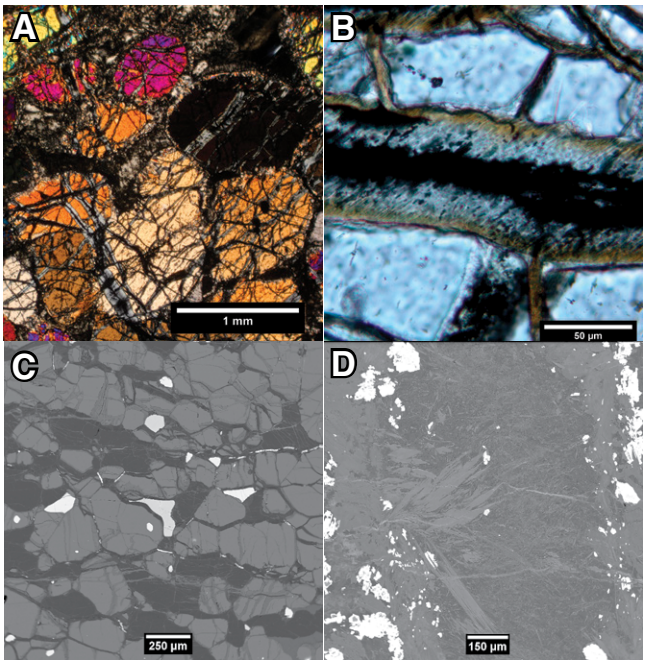

Figure 1. Photomicrographs illustrating the style of serpentinization within the Atlantis Massif (A,B) and electron micrographs illustrating the style of serpentinization within the Duluth Complex of the North American Mid-Continent Rift (C,D). Samples in A and B were prepared from the 1309D-241-R-2-33-36 and 1309D-235-R-2-5-8 intervals, which are just below and just above, respectively, the 241R1 and 235R2 samples. Sample imaged in C and D was prepared from the same hand sample as the Duluth Complex samples shown in Figure 2. Additional sample images are included in the Data Repository (Figs. DR1–DR3 [see footnote 1]).

National Institute of Standards and Technology Center for Neutron Research (NCNR; Maryland, USA). Rectangular neutron-absorbing Cd apertures were used to isolate individual regions of the samples. These samples and others from each sampling locality were additionally measured using larger, circular apertures, thus permitting bulk average measurements of the subsampled regions. To determine the individual samples' neutron scattering length densities (SLDs), which are a function of both chemical composition and density, we collected a variety of chemical analyses (Table DR1). Because of the large SLD contrast between solid materials and pore space (and/or water trapped as fluid inclusions), (U)SANS measurements of geologic samples can generally be approximated as a two-phase assemblage of mineral and pores. (U)SANS data were reduced and analyzed using the NCNR Igor macros (Kline, 2006), combined, and fit to remove incoherent background scattering. Using the PRINSAS software package (Hinde, 2004), the data were analyzed with a polydisperse spherical pore (PSP) model, and specific surface area (SSA) was calculated as a function of probe radius (in materials with pores covering multiple length scales, SSA is a function of the size of the probe used for the measurement) from the modeled PSP distributions. Calculated SSAs were extrapolated to a probe size of 4×10^{-10} m (the probe radius for N_2 gas) in order to compare between our calculated SSAs and literature SSAs measured by gas sorption (Table 1). Radlinski et al. (2004) estimated the combined uncertainty on the SSA model and extrapolation to be generally <±50%. Total porosities (ϕ, Table 1) within the measured pore size range were also calculated from the invariants of the scattering curves, which provide a model-independent estimate of the samples' ϕ. A detailed explanation of sample preparation, SLD calculations, and (U)SANS measurements is included in the Data Repository.

RESULTS AND DISCUSSION

The (U)SANS curves for the Atlantis Massif samples indicate an increase in scattering at high values of the scattering vector, Q, the region representative of the smallest pore radii (i.e., down to ~1–10 nm), with increasing abundance of serpentine and accessory phases (Fig. 2A; Fig. DR5A). Duluth Complex measurements similarly show increased scattering at high Q in the fractures relative to the wall rock and the inter-fracture matrix (Fig. 2B; Fig. DR5B). At values of Q representative of the largest pore sizes (i.e., up to ~10 µm), on the other hand, Atlantis Massif samples show generally decreasing scattering intensity with increasing alteration, consistent with the infilling of primary igneous pores with alteration phases. Within the Duluth Complex samples, the fractured samples scatter more intensely at low Q than the inter-fracture matrix, consistent with the abundance of micrometer- and larger-scale pores present within the fractures (Fig. 1D). The size and style of the analyzed Duluth Complex fractures are consistent with the extensional tectonics described by Foster and Hudleston (1986), which provided considerable volumes of fracture porosity independent of serpentinization-driven fracturing.

TABLE 1. POROSITIES AND SPECIFIC SURFACE AREAS (SSAs) CALCULATED FROM (ULTRA-) SMALL-ANGLE NEUTRON SCATTERING DATA

	Porosity ϕ (%)	SSA at radius 4 Å (m^2/g)
Atlantis Massif		
1309D-235-R-2-28-31	3.8	12
Region 1	3.6	0.4
Region 2	4.4	14
Region 3	3.2	8.8
Region 4	4.1	6.9
1309D-241-R-1-13-17	3.9	1.5
Duluth Complex		
Fracture	2.1	1.7
Wall rock	1.4	1.9
Inter-fracture matrix	1.4	0.08*
Wall rock + matrix	1.9	4.0
Fractured sample	1.8	0.67

*This SSA extrapolation ignores the value calculated for the lowest probe size, which is visually out of trend (Fig. 2).

Consistent with their surface fractal nature (Fig. 2), the modeled PSP distributions indicate that the majority of pores fall within the smallest examined pore size range, with the logarithm of the probability of a pore falling within a particular size range decaying with a slope of ~–3.1 to –3.7 with increasing logarithm of pore size. PRINSAS-calculated SSA distributions, which integrate sample-specific parameters (i.e., ϕ, ΔSLD) to place the analyses on a common, geologically meaningful reference scale (m^{-1}), allow for a more direct comparison between the individual measurements than the pore size distributions alone. The relative positions of the SSA curves calculated as a function of probe size for both the Atlantis Massif and Duluth Complex samples (Fig. 2) show that SSA created by pores with radii <~500 nm increases during serpentinization. Each individually analyzed region within the Atlantis Massif samples is an average of both primary and alteration textures, but the individual analyses clearly indicate that the proportion of pores with radii <~500 nm increases as the analyzed region is filled by a larger modal abundance of alteration minerals. This, therefore, can be taken as evidence that sub-micrometer pores are generated during serpentine formation. Larger-scale pores, i.e., those >~500 nm, are evidently characteristic of the primary igneous crystallization process, consistent with microstructural analyses (Wark et al., 2003). The SSA calculated for the full 235R2 sample indicates that it is approximately an average of the individually analyzed regions, which validates the smaller-scale measurements. The SSA calculated for the highly serpentinized 241R1 sample (Fig. DR2) is additionally in agreement with that of the highly serpentinized regions of sample 235R2.

The Duluth Complex samples offer a complementary set of observations. Whereas in the seafloor samples the serpentinization occurred along grain boundaries and in intragranular microfractures, the Duluth Complex serpentinization is largely confined to through-going fractures. Nonetheless, an important, corroborating result can be deduced from the relevant region

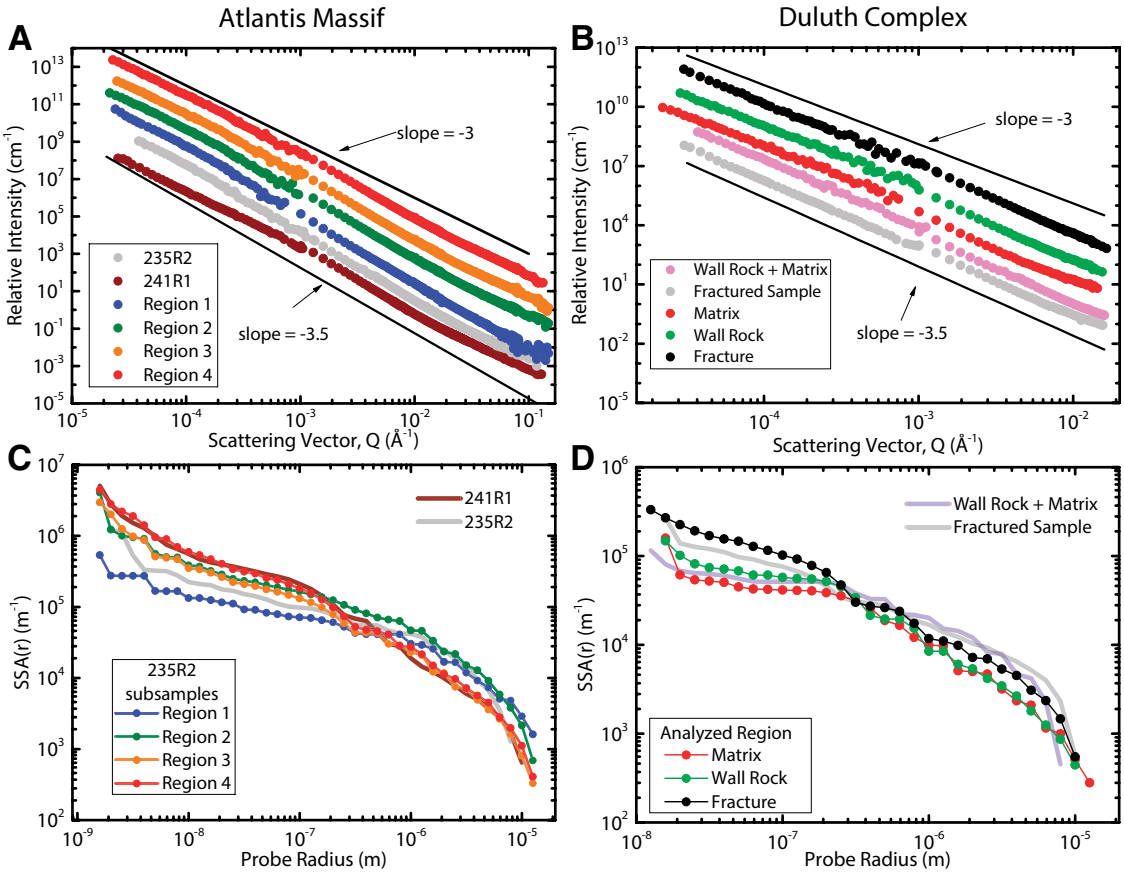

Figure 2. Results of (ultra-)small-angle neutron scattering analyses. Relative neutron scattering intensities are plotted as function of the scattering vector, *Q* (*Q* ~ 2π/*d*, where *d* is the scatterer diameter), for Atlantis Massif (A) and Duluth Complex (B) samples, and modeled specific surface area (SSA) of these samples is plotted as function of probe radius (*r*) in C and D, respectively. In A and B, each curve is offset by an order of magnitude, and lines with slopes representative of surface fractal scattering are plotted for comparison. Aperture size was varied to isolate sub-regions (lines + symbols in C, D) and larger regions (lines only in C, D) of samples. Atlantis Massif Regions 1, 2, 3, and 4 are composed of <10%, ~50%, ~50%, and ~60% alteration minerals, respectively (see Figs. DR1–DR3, Table DR1 [see footnote 1]).

of the fractured sample analyses, namely that pores with sizes <~500 nm are more abundant in the highly serpentinized fractures compared with the matrix and wall rock. Again, validation of these small-scale measurements is offered by the measurements performed with larger apertures, which behave as large-scale averages of the smaller regions. Extrapolating the calculated SSA curves to a probe size of 4×10^{-10} m and dividing by the sample density yields SSAs ranging from ~0.08–0.4 m^2/g for the least serpentinized regions to ~2–14 m^2/g for the more serpentinized regions (Table 1). These values compare favorably with values reported by Okland et al. (2014) for powdered samples of unaltered, partially altered, and highly altered dunite (1.7, 3.2, and 7.1 m^2/g, respectively).

Porosities calculated from the invariants of the scattering curves (Table 1) emphasize that the partially serpentinized samples we have analyzed indeed have significant porosity, up to ~4%. Importantly, the presented (U)SANS measurements account for both connected and unconnected porosity, which is present as fluid inclusions (Fig. DR4), but do not account for pores >~10 µm in size. Pore connectivity within the analyzed samples could potentially be constrained using SLD-matching (U)SANS experiments, but it is unclear whether such methods would produce more realistic assessments of the pore size distribution in actively serpentinizing rocks than those presented here. Pores and pore throats are continuously created and destroyed during serpentinization, and because serpentinization is expected to have ceased long before all analyzed rocks were sampled, the presented analyses are already ex-situ snapshots of this time-evolving process. (U)SANS experiments on rocks under pressure undergoing active serpentinization and deformation could greatly assist in the examination of the real-time evolution of serpentinite porosity.

Simultaneous consideration of Figure 2, Table 1, literature compilations of porosity and diffusivity measurements (e.g., Saad, 1969; Blackman et al., 2006; Macdonald and Fyfe, 1985), physics-based models (Jamtveit et al., 2008; Kelemen and Hirth, 2012), high-resolution characterization of serpentinizing interfaces (Plümper et al., 2012), and volumetric constraints (O'Hanley, 1996) indicates that the evolution of porosity and fluid flow during serpentinization is a process of coupled reaction, microfracture generation, porous phase infilling, and water diffusion through the neoformed, porous phases. Our (U)SANS measurements demonstrate that serpentine and accessory minerals form with their own inherent porosity, which is most likely associated with defects in serpentine and accessory phyllosilicates (Macdonald and Fyfe, 1985). Although this porosity is clearly integral to the serpentinization process, it has not yet been characterized with the level of detail offered by the (U)SANS techniques.

IMPLICATIONS

Porosity affects permeability in non-trivial ways, such that small changes in porosity and pore connectivity can significantly impact permeability (e.g., Davis et al., 2011). Therefore, knowledge of the evolution of porosity, pore sizes, and surface area with reaction progress is important for understanding the reactive-diffusive process of serpentinization. Apart from our (U)SANS analysis, several additional lines of evidence emphasize the importance of alteration-phase porosity in facilitating serpentinization reactions. Firstly, veinlet/microfracture width tends to increase with continued fluid flux (i.e., the conversion of type 1 to type 2 veins in Atlantis Massif troctolites; Beard et al., 2009), which must be permitted by flow and/or diffusion within the pores described here. Secondly, microfractures/veinlets that have seen longer periods of fluid flow also tend to have magnetite at their cores (Beard et al., 2009; Maffione et al., 2014; Fig. 1B). The formation of high-density magnetite (from early-formed ferroan brucite or serpentine) generates porosity by offsetting some of the volume increases associated with serpentine formation. Thirdly, measurements indicate that even highly serpentinized rocks have considerable porosity, which evolves with

reaction progress (e.g., Saad, 1969; Toft et al., 1990; Blackman et al., 2006).

Diffusion is a dominant mechanism for water and solute transport through serpentinites. Measured effective diffusion coefficients of water (D_{H_2O}) through serpentinized peridotites are ~10^{-7} to 10^{-8} cm^2/s (Macdonald and Fyfe, 1985), which are on the same order as those measured on partially weathered basalt (Navarre-Sitchler et al., 2009), suggesting a similar control on flow, transport, and reaction in both igneous rock types. Importantly, Navarre-Sitchler et al. (2009) showed that effective values of D_{H_2O} within weathered basalts are a function of the square of the basalt's connected porosity. Assuming a similar dependence for serpentinizing peridotite, porosity increases with serpentinization progress will exponentially increase the effective D_{H_2O} of serpentinites and exponentially increase serpentinization rates as serpentinization intensity increases, so long as the temperatures remain thermodynamically and kinetically favorable. Therefore, the (U)SANS measurements and analyses we have presented offer nanoscale quantification of the first-order controls on fluid migration and serpentinization rates associated with porosity generated through reaction-driven, hierarchical fracturing. Future studies coupling (U)SANS and transmission electron microscopy characterization of the alteration phase–hosted pores can offer further insight into their evolution with reaction progress.

ACKNOWLEDGMENTS

Funding was provided by the U.S. Department of Energy and the U.S. National Science Foundation (NSF) under grants EE0002764 and 1426695, respectively, and a University of Minnesota (UMN) Doctoral Dissertation Fellowship and Geological Society of America research grant to Tutolo. Saar thanks the George and Orpha Gibson Endowment for supporting the Hydrogeology and Geofluids research group at UMN and this project. Jim Miller and John Green are thanked for field assistance. This work utilized samples and data provided by the IODP. (U)SANS instrumentation is supported in part by the NSF under agreement DMR-0944662. Any mention of commercial products is for information only; it does not imply recommendation or endorsement by the National Institute of Standards and Technology. Oliver Plümper, Bob Lowell, and Norman Sleep are thanked for their helpful reviews.

REFERENCES CITED

Anovitz, L.M., Lynn, G.W., Cole, D.R., Rother, G., Allard, L.F., Hamilton, W.A., Porcar, L., and Kim, M.-H., 2009, A new approach to quantification of metamorphism using ultra-small and small angle neutron scattering: Geochimica et Cosmochimica Acta, v. 73, p. 7303–7324, doi:10.1016/j.gca.2009.07.040.

Barker, J.G., Glinka, C.J., Moyer, J.J., Kim, M.H., Drews, A.R., and Agamalian, M., 2005, Design and performance of a thermal-neutron double-crystal diffractometer for USANS at NIST: Journal of Applied Crystallography, v. 38, p. 1004–1011, doi:10.1107/S0021889805032103.

Beard, J.S., Frost, B.R., Fryer, P., McCaig, A., Searle, R., Ildefonse, B., Zinin, P., and Sharma, S.K., 2009, Onset and progression of serpentinization and magnetite formation in olivine-rich troctolite from IODP Hole U1309D: Journal of Petrology, v. 50, p. 387–403, doi:10.1093/petrology/egp004.

Blackman, D.K., Ildefonse, B., John, B.E., Ohara, Y., Miller, D.J., MacLeod, C.J., and the Expedition 304/305 Scientists, 2006, Proceedings of the Integrated Ocean Drilling Program, Volume 304/305: Oceanic Core Complex Formation, Atlantis Massif: College Station, Texas, Integrated Ocean Drilling Program Management International, Inc., doi:10.2204/iodp.proc.304305.2006.

Davis, M.A., Walsh, S.D.C., and Saar, M.O., 2011, Statistically reconstructing continuous isotropic and anisotropic two-phase media while preserving macroscopic material properties: Physical Review E: Statistical, Nonlinear, and Soft Matter Physics, v. 83, 026706, doi:10.1103/PhysRevE.83.026706.

Foster, M.E., and Hudleston, P.J., 1986, "Fracture cleavage" in the Duluth Complex, northeastern Minnesota: Geological Society of America Bulletin, v. 97, p. 85–96, doi:10.1130/0016-7606(1986)97<85:FCITDC>2.0.CO;2.

Glinka, C.J., Barker, J.G., Hammouda, B., Krueger, S., Moyer, J.J., and Orts, W.J., 1998, The 30 m small-angle neutron scattering instruments at the National Institute of Standards and Technology: Journal of Applied Crystallography, v. 31, p. 430–445, doi:10.1107/S0021889897017020.

Hinde, A.L., 2004, PRINSAS: A Windows-based computer program for the processing and interpretation of small-angle scattering data tailored to the analysis of sedimentary rocks: Journal of Applied Crystallography, v. 37, p. 1020–1024, doi:10.1107/S0021889804021260.

Jamtveit, B., Malthe-Sørenssen, A., and Kostenko, O., 2008, Reaction enhanced permeability during retrogressive metamorphism: Earth and Planetary Science Letters, v. 267, p. 620–627, doi:10.1016/j.epsl.2007.12.016.

Kelemen, P.B., and Hirth, G., 2012, Reaction-driven cracking during retrograde metamorphism: Olivine hydration and carbonation: Earth and Planetary Science Letters, v. 345–348, p. 81–89, doi:10.1016/j.epsl.2012.06.018.

Kelley, D.S., et al., 2005, A serpentinite-hosted ecosystem: The Lost City hydrothermal field: Science, v. 307, p. 1428–1434, doi:10.1126/science.1102556.

Klein, F., Humphris, S.E., Guo, W., Schubotz, F., Schwarzenbach, E.M., and Orsi, W.D., 2015, Fluid mixing and the deep biosphere of a fossil Lost City–type hydrothermal system at the Iberia Margin: Proceedings of the National Academy of Sciences of the United States of America, v. 112, p. 12,036–12,041, doi:10.1073/pnas.1504674112.

Kline, S.R., 2006, Reduction and analysis of SANS and USANS data using IGOR Pro: Journal of Applied Crystallography, v. 39, p. 895–900, doi:10.1107/S0021889806035059.

Macdonald, A.H., and Fyfe, W.S., 1985, Rate of serpentinization in seafloor environments: Tectonophysics, v. 116, p. 123–135, doi:10.1016/0040-1951(85)90225-2.

Maffione, M., Morris, A., Plümper, O., and van Hinsbergen, D.J., 2014, Magnetic properties of variably serpentinized peridotites and their implication for the evolution of oceanic core complexes: Geochemistry Geophysics Geosystems, v. 15, p. 923–944, doi:10.1002/2013GC004993.

Martin, B., and Fyfe, W.S., 1970, Some experimental and theoretical observations on the kinetics of hydration reactions with particular reference to serpentinization: Chemical Geology, v. 6, p. 185–202, doi:10.1016/0009-2541(70)90018-5.

Navarre-Sitchler, A., Steefel, C.I., Yang, L., Tomutsa, L., and Brantley, S.L., 2009, Evolution of porosity and diffusivity associated with chemical weathering of a basalt clast: Journal of Geophysical Research, v. 114, F02016, doi:10.1029/2008JF001060.

Navarre-Sitchler, A.K., Cole, D.R., Rother, G., Jin, L., Buss, H.L., and Brantley, S.L., 2013, Porosity and surface area evolution during weathering of two igneous rocks: Geochimica et Cosmochimica Acta, v. 109, p. 400–413, doi:10.1016/j.gca.2013.02.012.

O'Hanley, D.S., 1996, Serpentinites: Oxford, UK, Oxford University Press, 277 p.

Okland, I., Huang, S., Thorseth, I.H., and Pedersen, R.B., 2014, Formation of H_2, CH_4 and N-species during low-temperature experimental alteration of ultramafic rocks: Chemical Geology, v. 387, p. 22–34, doi:10.1016/j.chemgeo.2014.08.003.

Plümper, O., Røyne, A., Magrasó, A., and Jamtveit, B., 2012, The interface-scale mechanism of reaction-induced fracturing during serpentinization: Geology, v. 40, p. 1103–1106, doi:10.1130/G33390.1.

Radlinski, A.P., Mastalerz, M., Hinde, A.L., Hainbuchner, M., Rauch, H., Baron, M., Lin, J.S., Fan, L., and Thiyagarajan, P., 2004, Application of SAXS and SANS in evaluation of porosity, pore size distribution and surface area of coal: International Journal of Coal Geology, v. 59, p. 245–271, doi:10.1016/j.coal.2004.03.002.

Saad, A.H., 1969, Magnetic properties of ultramafic rocks from Red Mountain, California: Geophysics, v. 34, p. 974–987, doi:10.1190/1.1440067.

Seyfried, W.E., Pester, N.J., Tutolo, B.M., and Ding, K., 2015, The Lost City hydrothermal system: Constraints imposed by vent fluid chemistry and reaction path models on subseafloor heat and mass transfer processes: Geochimica et Cosmochimica Acta, v. 163, p. 59–79, doi:10.1016/j.gca.2015.04.040.

Sleep, N.H., Meibom, A., Fridriksson, T., Coleman, R.G., and Bird, D.K., 2004, H_2-rich fluids from serpentinization: Geochemical and biotic implications: Proceedings of the National Academy of Sciences of the United States of America, v. 101, p. 12,818–12,823, doi:10.1073/pnas.0405289101.

Toft, P.B., Arkani-Hamed, J., and Haggerty, S.E., 1990, The effects of serpentinization on density and magnetic susceptibility: A petrophysical model: Physics of the Earth and Planetary Interiors, v. 65, p. 137–157, doi:10.1016/0031-9201(90)90082-9.

Wark, D.A., Williams, C.A., Watson, E.B., and Price, J.D., 2003, Reassessment of pore shapes in microstructurally equilibrated rocks, with implications for permeability of the upper mantle: Journal of Geophysical Research, v. 108, 2050, doi:10.1029/2001JB001575.

Weiblen and Morey, 1980, A summary of the stratigraphy, petrology, and structure of the Duluth Complex: American Journal of Science, v. 280-A, p. 88–133.

Manuscript received 10 September 2015
Revised manuscript received 25 November 2015
Manuscript accepted 30 November 2015

Printed in USA